Energy & Environmental Science

Cite this: *Energy Environ. Sci.*, 2011, **4**, 4252

www.rsc.org/ees

PAPER

Nanoprobe X-ray fluorescence characterization of defects in large-area solar cells†

M. I. Bertoni,*[a] D. P. Fenning,[a] M. Rinio,[b] V. Rose,[c] M. Holt,[d] J. Maser[d] and T. Buonassisi[a]

Received 6th July 2011, Accepted 27th July 2011
DOI: 10.1039/c1ee02083h

The performance of centimeter-sized energy devices is regulated by inhomogeneously distributed nanoscale defects. To improve device efficiency and reduce cost, accurate characterization of these nanoscale defects is necessary. However, the multiscale nature of this problem presents a characterization challenge, as non-destructive techniques often specialize in a single decade of length scales, and have difficulty probing non-destructively beneath the surface of materials with sub-micron spatial resolution. Herein, we push the resolution limits of synchrotron-based nanoprobe X-ray fluorescence mapping to 80 nm, to investigate a recombination-active intragranular defect in industrial solar cells. Our nano-XRF measurements distinguish fundamental differences between benign and deleterious dislocations in solar cell devices: we observe recombination-active dislocations to contain a high degree of nanoscale iron and copper decoration, while recombination-inactive dislocations appear clean. Statistically meaningful high-resolution measurements establish a connection between commercially relevant materials and previous fundamental studies on intentionally contaminated model defect structures, pointing the way towards optimization of the industrial solar cell process. Moreover, this study presents a hierarchical characterization approach that can be broadly extended to other nanodefect-limited energy systems with the advent of high-resolution X-ray imaging beamlines.

1. Introduction

Industrial conversion efficiencies of quantum energy devices, such as solar cells, are far from their theoretical maxima.[1,2,9–11] The performance of a device hundreds of square centimeters in area is often limited by nanoscale defects.[9–11] These defects affect electron transport, causing macroscopic current inhomogeneities, low breakdown voltages, and shunts.[12,13] In multicrystalline silicon (mc-Si) solar cells, structural defects such as dislocations and grain boundaries[14,15] are known to act as enhanced recombination centers. Dislocations are particularly detrimental, because these intragranular defects cover a large area fraction of the photovoltaic devices.[16–18] Reports have suggested that the electrical activity of dislocations is directly related to their interaction with segregated impurities rather than merely from dangling bonds.[3–8,19–23] However, the direct correlation between the electrical activity and the local defect structure has proven to be particularly challenging, since it requires analytical tools with high spatial resolution and the ability to sample a large volume of the material. Many of these nanoscale structural defects are tens of microns apart, inhomogeneously distributed over a hundred-square-centimeter surface area. The multiscale nature

[a]*Massachusetts Institute of Technology, Cambridge, MA, 02139, USA. E-mail: mbertoni@mit.edu*
[b]*Fraunhofer ISE, Laboratory and Servicecenter, Auf der Reihe 2, 45884 Gelsenkirchen, Germany*
[c]*Advanced Photon Source, Argonne National Laboratory, Argonne, IL, 60439, USA*
[d]*Center for Nanoscale Materials, Argonne National Laboratory, Argonne, IL, 60439, USA*

† Electronic Supplementary Information (ESI) available: Complementary XRF maps and ICPMS table. See DOI: 10.1039/c1ee02083h.

Broader context

The performance of energy-conversion devices is often regulated by inhomogeneously distributed nanoscale defects. To improve device efficiency and reduce production costs, it is essential to engineer and control these defects. However, the multiscale nature of this problem, spanning over seven decades of length scale, presents a characterization challenge. In this work, we describe a new approach for bridging the gap between the macroscopic electrical response of an industrial solar cell and the nano-sized impurities that govern its performance. We report the use of an advanced synchrotron-based X-ray fluorescence nanoprobe with resolution limits below 80 nm to investigate the elemental natures of recombination-active intragranular defects in industrial solar cells.

of this problem presents a challenge to traditional characterization techniques, which often specialize in one decade of length scales. In particular, accurate non-destructive compositional characterization below the micron threshold has been out of reach.

Up to now, the imaging techniques of choice, such as electron beam induced current (EBIC) have proven to be limited to spatial resolutions of a couple of microns due to electron matrix scattering.[3,24,25] Only transmission electron microscopy (TEM) studies have been able to show a fine dispersion of impurities along dislocations on the nanometer scale.[18,23,26] However, due to the small sampling areas in TEM specimens and the complexity of destructive sample preparation, samples must often be intentionally contaminated, and resulting measurements lack representative sampling sizes for industrial solar cell applications. X-Ray fluorescence and its most recent electrical characterization complements like X-ray Beam Induced Current (XBIC)[3,27] and X-ray beam excited optical luminescence microscopy (SXEOL)[10,28] have been valuable in bridging this length scale gap. However, until recently this suite of X-ray techniques has been limited to resolutions above a hundred nanometers.[29–31] With sub-100 nm spatial resolution, it is expected that smaller intragranular defects can be detected.[32] Fig. 1 illustrates the impact a hard X-ray nanoprobe with a spatial resolution of below 100 nm could have within the broader spectrum of these non-destructive analytical tools.

In this work, we exploit this last decade of length scale, which has been previously unreachable with standard hard X-ray probe beamlines. Using the synchrotron-based Hard X-ray nanoprobe (HXN) operated by the Centre for Nanoscale Materials at Argonne National Laboratory's Advanced Photon Source beamline 26-ID, we probe for the first time the elemental natures of nanoscale defects at intragranular dislocations in a commercial mc-Si material with a beam spot size of 80 nm. The results distinguish underlying differences between benign and deleterious dislocations in a solar cell device.

2. Discussion

Fig. 2 shows a laser-beam induced current (LBIC) map of a quarter of a mc-Si solar cell device and the two chosen regions of interest (ROI), A and B, where darker and lighter regions correspond to underperforming and high-performance areas of the device, respectively. To identify the nature of the defect(s) responsible for poor local performance, the samples were etched to highlight structural defects (Fig. 2b). Notice that all of the underperforming areas correspond to the position of grain boundaries and dislocations. Furthermore, in intragranular areas with comparable dislocation densities, one observes a range of electrical impacts. While elegant models of recombination activity as a function of impurity decoration have been presented for intentionally contaminated misfit dislocations and stacking faults,[21,22] what properties determine dislocation recombination in commercially relevant industrial solar cells has been a long-standing question in the field.[23–28]

Dislocation recombination activity can be quantified using the dimensionless parameter, Γ, usually referred to as the normalized recombination strength or gamma factor. We note that $\Gamma = \gamma/D$, where D is the minority carrier diffusion coefficient and γ is the recombination strength defined as the number of recombinations per time, unit length and excess carrier density. To correlate electrical performance with defect density on the micron scale, LBIC and dislocation density (ρ) maps were registered and compared. Using Donolato's dislocation model[24] combined with one-dimensional solar cell device modeling (PC1D[33]) we obtained pixel-by-pixel estimates of internal quantum efficiency as a function of dislocation density, IQE(ρ). The gamma factor (Γ) is obtained by fitting the theoretical IQE(ρ) to the measured

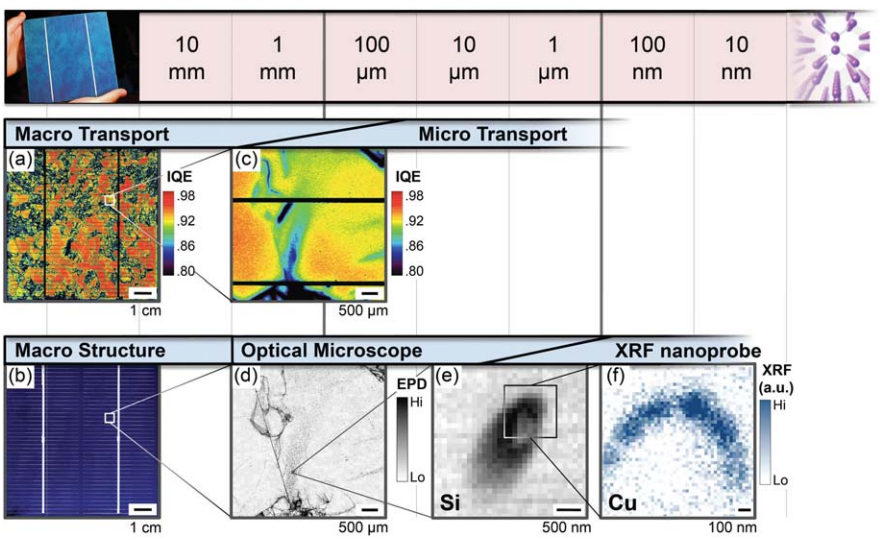

Fig. 1 Hierarchical material characterization from centimeters to nanometers. (a) Full-wafer internal quantum efficiency (IQE) map, illustrating high- and low-performance areas. (b) Such data is imperceptible in a full-wafer reflected light image. (c) A region of interest is shown in greater detail, highlighting high- and low-performance areas with micron-scale resolution. (d) Optical microscope image of etched sample indicates dislocations present at intragranular regions of high recombination activity. (e) Nano-XRF is used to map the dislocation etch pits. The silicon channel is surface-sensitive, thus yielding topographical information. (f) A region of the etch pit is selected for high-resolution nano-XRF, indicating that copper is present at the dislocation.

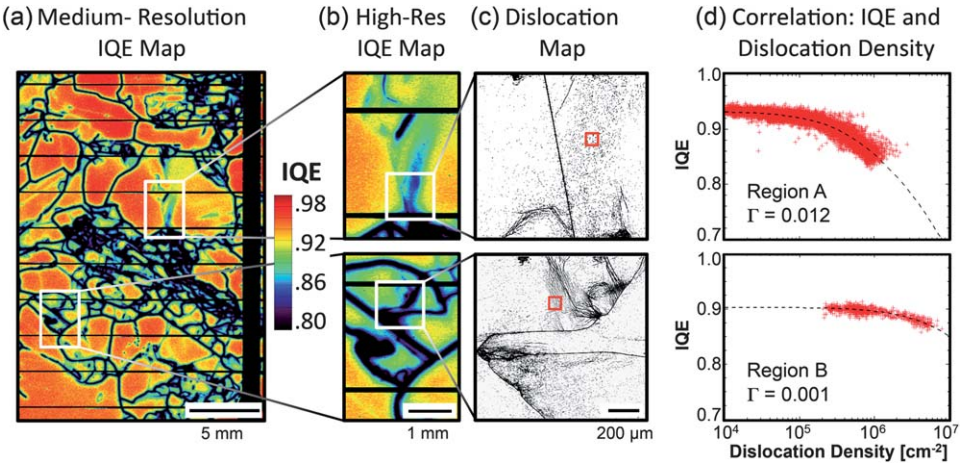

Fig. 2 Deleterious and benign dislocation types distinguished by nano-XRF. (a) A medium-resolution IQE map, highlighting (b) two regions of interest. (c) Dislocation etch pit maps indicate that underperforming regions correspond to regions of high dislocation density. (d) Quantitative pixel-by-pixel correlation between IQE and dislocation density in (b) indicates that Region A contains strongly recombination-active dislocations (deleterious), while Region B contains dislocations with an order of magnitude lower recombination activity (comparatively benign). The red squares in (c) indicate regions selected for nano-XRF analysis, shown in Fig. 3.

data. The resulting IQE *vs.* ρ curves for Regions A and B are presented in Fig. 2(d), where it can be observed that Region A has a much higher gamma factor ($\Gamma = 1.2 \times 10^{-2}$) than Region B ($\Gamma = 9 \times 10^{-4}$), indicating a more than 10× increase of dislocation recombination strength. The origin of low and high gamma factors has been a subject of debate. Recently Rinio *et al.*[26] observed a single high gamma dislocation by TEM and found it heavily decorated with oxygen precipitates, while a single low gamma dislocation in the same sample was decorated by only a few, small precipitates. The authors noted that the lack of a statistically meaningful sample size inhibits the inference of firm conclusions on the origin of dislocation recombination activity. At the HXN, we chose a photon energy of 10 keV to allow identification and mapping of transition metal impurities up to Cu and Zn at and near dislocations. We observed a clear distinction between dislocations of high and low recombination activity (gamma factor). Fig. 3(a) shows four XRF maps obtained at dislocation etch pits in Region A (high gamma factor). Elemental distribution maps show the clustering of Fe and Cu precipitates around these dislocation pits. Of the four etch pits sampled in this recombination-active region, three were decorated by metallic impurities, mostly Cu, Fe and Ca. Fig. 3(a) presents the Cu and Fe maps since they are known to be detrimental to the performance of silicon solar cells,[9,10] Ca maps can be found in the ESI †. The colormaps of all Cu and Fe elemental XRF maps shown were scaled between one standard deviation (black level) and four standard deviations (white level) above the mean signal over the map area to emphasize clusters where metal concentrations were significantly above the background signal. Fig. 3(b) presents the XRF maps around four etch pits in the low gamma region, revealing no evidence of metal precipitation. A total of eleven etch pits were evaluated in this low-recombination Region B all of which showed no metal content above the sensitivity of the beamline.

A high-resolution map, shown in Fig. 4(a), was taken around a heavily contaminated area of etch pit II from Region A with a 25 nm step size. The Cu XRF scale bar shows values of loading

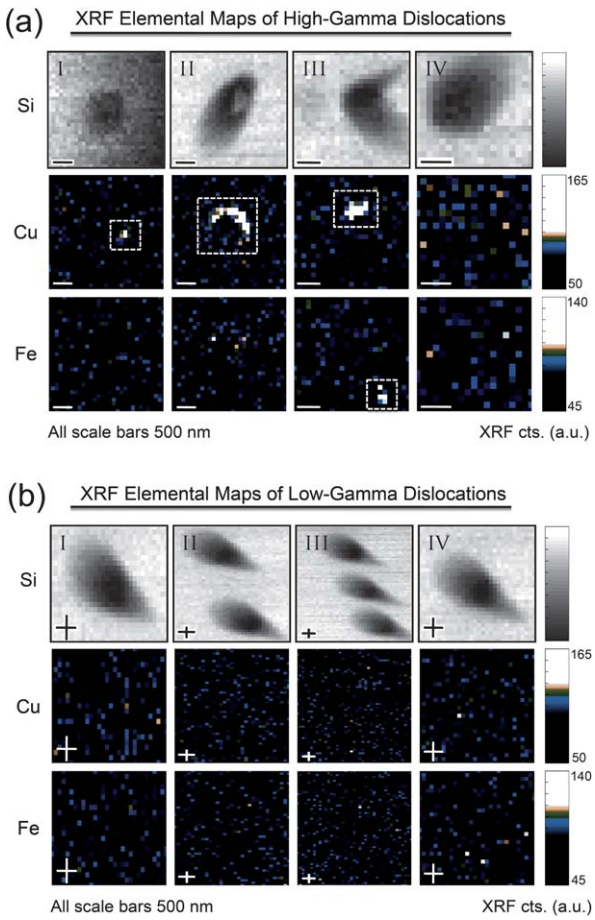

Fig. 3 Nano-XRF detects metals at recombination-active dislocations. (a) Four dislocation etch pits from Region A, which contains recombination-active dislocations. In nano-XRF maps, three out of the four etch pits exhibit metal contamination, namely copper and iron. (b) Four representative etch pits from Region B, which contains benign dislocations. Eleven etch pits were analyzed in total, and not one exhibited significant metal contamination.

concentrations (μg cm^{-2}) estimated from measurements of Si samples and NIST standard reference materials 1832 and 1833 taken at the Advanced Photon Source beamline 2-ID-D. Concentrations should be accurate to within an order of magnitude, due to necessary approximations made in the analysis.

Fig. 4(b) illustrates the beam profile given by linescans on a 10 nm Cr film sectioned and scanned edge on, here the blue line corresponds to the zone plate used in this study (FWHM $\sim$ 80 nm). The dashed line demonstrates the highest resolution possible (FWHM $\sim$ 40 nm) with the hard X-ray nanoprobe (HXN) using a state-of-the-art zone plate lens. To provide a higher photon flux, we used a zone plate with lower resolution, higher focusing efficiency, and similar lineshape for the trace element analysis. The efficiency for this zone plate relative to a 1000 mm^2 parallel beam at 8 keV is 4.34% with a focused flux of 5.2×10^8 photon s^{-1}.

We observe that some of the metals illustrated in Fig. 3 appear to follow the contour of the etch pit. It is possible that these XRF maps reveal the remainder of an impurity cloud induced by the dislocation strain field[34,35] that was not removed by defect etching, or perhaps the metals are precipitated around silicon oxide precipitates. Given our cleaning protocol and the precautions to prevent unintentional contamination (see Methods), it is unlikely the metals are an artifact of contamination.

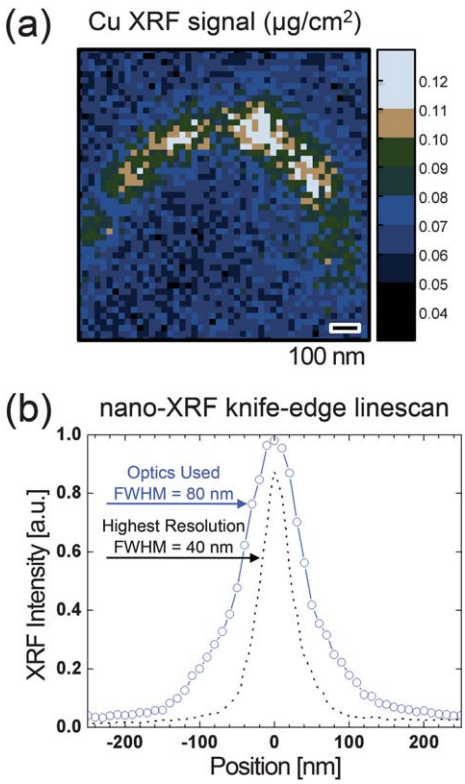

Fig. 4 High-resolution, hard X-ray nanoprobe spot. (a) XRF map of a dislocation etch pit showing metal decoration at the highest resolution achievable, scale bar shows concentration loading (μg cm^{-2}). (b) Knife-edge linescan showing spot size achieved with the high flux optics used in this experiment (blue) compared to the highest resolution optic available (black) at BL26.

Furthermore, the fact that Region B of the same sample appears completely devoid of metallic impurities indicates sample preparation did not contaminate the surfaces. We thus have high confidence that observed impurities are contained in the bulk of the solar cell. These results support the hypothesis that nanoscale metal impurities regulate the recombination activity of dislocations in industrial mc-Si material. The findings are consistent with experiments on intentionally-contaminated Si/SiGe misfit dislocation model defect structures that demonstrate an increase of a/2 <110> misfit dislocation recombination activity with metal contamination.[3–6,36,37]

Why Cu, Fe and Ca are associated with recombination-active dislocations remains an open question. At growth temperatures immediately following solidification, all metal atoms should be dissolved uniformly throughout the bulk. As the temperature drops, supersaturated metals should precipitate at the most energetically favorable heterogeneous nucleation sites, including dislocations. It has been proposed that dislocation metal decoration may increase with residence time,[26] such that the earliest dislocations to form are the most decorated. This would require metal precipitation to be energetically favorable at elevated temperatures, *i.e.*, the presence of impurities in the silicon at higher concentrations than their solubility at the temperatures where the dislocations are generated. Simulations suggest that most dislocations form above 1000 °C during the cooling of a mc-Si ingot.[38–40] At 1000 °C, the solid solubilities in silicon of Cu and Fe are 5×10^{17} and 4×10^{14} cm^{-3}, respectively.[41] Inductively coupled plasma mass spectrometry (ICPMS) results on an adjacent as-grown (unprocessed) sister wafer show that the concentrations of Cu ($<1 \times 10^{13}$ cm^{-3}) and Fe (1×10^{14} cm^{-3}) are well below these solubility limits, which suggests that metal precipitation occurred after all dislocations had formed.† Thus one can conclude, that the difference in decoration between the high and low gamma regions is not driven by the amount of time the dislocations have been in the wafer. Another potential explanation of our experimental observations could be a difference in dislocation microstructure between Region A and Region B. Dislocations formed earlier during the crystallization process are known to exhibit a higher degree of disorder (kinks, jogs, tangles), as dislocation mobility, dislocation climb, and kink formation probability are all favored at high temperature.[42] On the contrary, dislocations formed later in the crystallization process present a much more ordered structure, mainly because they do not have the thermal energy necessary to climb and jog, and their movement is constrained to glide along glide planes.[26] The metal precipitate nucleation energy barrier could be lower at dislocations in Region A due to a difference in dislocation microstructure, following a similar trend to that observed at different types of grain boundaries.[14,43] Optical exploration as well as X-ray fluorescence maps of the dislocation etch pits (see Si maps of Fig. 3(a) and 3(b)) indicate a systematic difference in etch pit shape and size consistent with this hypothesis. Whereas Region B (low recombination activity) contains orderly dislocation etch pits of circular shape and similar orientation (Fig. 3 (a), Si maps), Region A (high recombination activity) contains widely varying dislocation etch pit types (Fig. 3(b), Si maps). It is possible that the more disordered dislocation distribution of Region A originates as a consequence of oxygen precipitates locking the dislocations in place,[44] in agreement with recent

observations by Rinio *et al.*[26] It is also possible that the distinct microstructure of these two regions governs the gettering behavior of the decorating impurities, whereas the dislocations in Region B contain more energetically favorable heterogeneous nucleation sites than dislocations in Region A. Further investigation of dislocation microstructure, perhaps by scanning nanobeam diffraction[45] or TEM, may yield further insights into these questions.

3. Methods

A 10 × 10 cm^2 solar cell was processed from standard mc-Si (multicrystalline silicon) following the steps described for wafer number 1 in ref. 45 (Fig 1(a)). A map of current collection efficiency was measured over the entire device with a spatial resolution of 50 μm using the laser beam induced current (LBIC) technique with a single laser wavelength of 832 nm at an injection level of approximately AMl.5 with no bias light. High-resolution LBIC maps were obtained in underperforming regions with a spatial resolution of 12.5 μm. Samples were polished on both sides, removing the contacts and the emitter. A one-minute Secco etch[46] was used to reveal structural defects (dislocations and grain boundaries). An area of approximately 25 mm^2 was photographed with an optical microscope with a resolution of approximately 700 nm. The positions of all etch pits were acquired by an automatic image processing system to obtain the local dislocation density, ρ. To correlate electrical performance with defect density on the micron scale, LBIC and ρ maps were registered and compared pixel by pixel with a spatial resolution of 12.5 μm. By means of PC1D, maps of IQE as a function of diffusion length (L) can be calculated.[33] All known properties of the solar cell (emitter profile, sample thickness, surface recombination velocities, *etc.*) and the wavelength of the incident light were taken into account in this step. Combining Donolato's dislocation model $L(\rho)$ with the PC1D model for IQE(L) of the solar cell we obtained a function of the form $IQE_{\Gamma, L_0}(\rho)$, where L_0 is the diffusion length of the dislocation free bulk and the values of Γ and L_0 are consistently varied until the function best represents the experimental data. This fitting procedure reveals the normalized recombination strength, Γ, of the dislocations.[24] For more details regarding this technique see ref. 26,47. The ROIs were studied in phosphorous diffused sample by synchrotron-based X-ray fluorescence microscopy (XRF) to characterize the elemental distribution of metallic impurities in the material. Samples were RCA cleaned using standard SC1 and SC2 solutions; dips in hydrofluoric acid (10%) were performed in between baths and after the cleaning to eliminate the surface oxide layer. A gold grid commonly used for transmission electron microscopy (TEM) with a 100 μm opening was mounted on the upstream side (facing the incident X-ray beam) to easily locate the ROIs by means of a transmission image. The hard X-ray nanoprobe beamline at the Advanced Photon Source, sector 26-ID, Argonne National Laboratory, allows analysis of major and minor elemental constituents in a small sample region probed by a focused X-ray beam. Fresnel zone plates with an outermost zone width of 45 nm and an acceptance of 160 μm are used to focus X-rays with a photon energy of 10 keV to a spot size of approximately 80 nm. The depth of focus is 40 μm. We scanned the X-ray probe with a step size as small as 25 nm. A laser interferometer positioning system provided position feedback with an accuracy of 5 nm. ICP-MS analysis was performed by Applied Materials ChemTrace Analytical Testing Services. Surface contamination was removed by chemically etching several microns before full digestion and analysis.

4. Conclusions

In summary, synchrotron-based nanoprobe X-ray fluorescence with 80 nm spatial resolution has been used to map large-area industrial solar cells, distinguishing the fundamental differences between benign and deleterious dislocations in these devices. What causes the difference in recombination activity of dislocation clusters has been difficult to address given the limited spatial resolution of most common analytical tools, the destructive nature of others, and the intrinsic multiscale nature of the problem. We present here a non-destructive hierarchical imaging methodology that locates regions of interest at the centimeter scale and probes elemental composition with 25 nm steps, leveraging the state-of-the-art X-ray fluorescence nanoprobe. We observe that recombination-active dislocations contain a high amount of nanometer-sized iron and copper particles, while recombination-inactive dislocations present no metal impurity decoration above the detection limits. With the X-ray community pursuing higher spatial resolutions and sensitivities, this approach has the potential to address a wide range of problems pertaining to inhomogeneously distributed nanoscale defect science, including organic and inorganic thin-film solar cells, batteries, heterogeneous catalysis, thermoelectric devices, and next-generation nanoelectronics.

5. Acknowledgements

The authors thank Martin Kaes from the University of Konstanz for helping with sample preparation. This work was supported by the U.S. Department of Energy under contract number DE-FG36-09GO19001, and a generous gift from the Chesonis Family Foundation. D. P. Fenning acknowledges the support of a National Science Foundation Graduate Research Fellowship. Beamline operational funding is provided by the U.S. Department of Energy, Office of Science, Office of Basic Energy Sciences, under contract DEAC02-06CH11357.

References

1 T. Tiedje, E. Yablonovitch, G. Cody and B. Brooks, *IEEE Trans. Electron. Dev.*, 2005, **31**, 711–716.
2 G. Araújo and A. Martí, *Sol. Energy Mater. Sol. Cells*, 1994, **33**, 213–240.
3 T. Fell, P. Wilshaw and M. de Coteau, *Phys. Status Solidi A*, 1993, **138**, 695–704.
4 D. Lee and G. Rozgonyi, *Appl. Phys. Lett.*, 1994, **65**, 350–352.
5 M. Kittler, C. Ulhaq-Bouillet and V. Higgs, *J. Appl. Phys.*, 1995, **78**, 4573–4583.
6 O. Vyvenko, T. Buonassisi, A. Istratov, E. Weber, M. Kittler and W. Seifert, *J. Phys.: Condens. Matter*, 2002, **14**, 13079–13086.
7 M. de Coteau, P. Wilshaw and R. Falster, *Phys. Status Solidi A*, 1990, **117**, 403–408.
8 M. Seibt, H. Hedemann, A. Istratov, F. Riedel, A. Sattler and W. Schrter, *Phys. Status Solidi A*, 1999, **171**, 301–310.
9 J. Davis, A. Rohatgi, R. Hopkins, P. Blais, P. Rai-Choudhury, J. McCormick and H. Mollenkopf, *IEEE Trans. Electron. Dev.*, 1980, **27**, 677–687.

10 S. Riepe, I. E. Reis, W. Kwapil, M. A. Falkenberg, J. Schön, H. Behnken, J. Bauer, D. Kreßner-Kiel, W. Seifert and W. Koch, *Phys. Status Solidi C*, 2011, **8**, 733–738.
11 T. Buonassisi, A. Istratov, M. Marcus, M. Heuer, M. Pickett, B. Lai, Z. Cai, S. M. Heald and E. Weber, *Solid State Phenom.*, 2005, **108–109**, 577–584.
12 J. Isenberg and W. Warta, *Progr. Photovolt.: Res. Appl.*, 2004, **12**, 339–353.
13 T. Buonassisi, O. Vyvenko, A. Istratov, E. Weber, G. Hahn, D. Sontag, J. Rakotoniaina, O. Breitenstein, J. Isenberg and R. Schindler, *J. Appl. Phys.*, 2004, **95**, 1556.
14 J. Chen, T. Sekiguchi, D. Yang, F. Yin, K. Kido and S. Tsurekawa, *J. Appl. Phys.*, 2004, **96**, 5490.
15 G. Stokkan, S. Riepe, O. Lohne and W. Warta, *J. Appl. Phys.*, 2007, **101**, 053515.
16 K. Nakayashiki, V. Meemongkolkiat and A. Rohatgi, *IEEE Trans. Electron. Dev.*, 2005, **52**, 2243.
17 J. Isenberg, J. Dicker and W. Warta, *J. Appl. Phys.*, 2003, **94**, 4122.
18 B. Sopori and W. Chen, *J. Cryst. Growth*, 2000, **210**, 375–378.
19 C. Cabanel and J. Laval, *J. Appl. Phys.*, 1990, **67**, 1425–1432.
20 S. Pizzini, A. Sandrinelli, M. Beghi, D. Narducci, F. Allegretti, S. Torchio, G. Fabbri, G. Ottaviani, F. Demartin and A. Fusi, *J. Electrochem. Soc.*, 1988, **135**, 155–165.
21 P. Wilshaw and T. Fell, *Journal de Physique IV*, 1991, **1**, 3–14.
22 V. Kveder, M. Kittler and W. Schröter, *Phys. Rev. B: Condens. Matter Mater. Phys.*, 2001, **63**, 11.
23 M. Seibt, V. Kveder, W. Schroeter and O. Voss, *Phys. Status Solidi A*, 2005, **202**, 911–920.
24 C. Donolato, *J. Appl. Phys.*, 1998, **84**, 2656–2664.
25 J. Lu, G. Rozgonyi and A. Schönecker, *Mater. Sci. Semicond. Process.*, 2008, **11**, 20–24.
26 M. Rinio, A. Yodyungyong, S. Keipert-Colberg, D. Borchert and A. Montesdeoca-Santana, *Phys. Status Solidi A*, 2011, **208**, 760–768.
27 O. Vyvenko, T. Buonassisi, A. Istratov and E. Weber, *J. Phys.: Condens. Matter*, 2004, **16**, S141–S151.
28 O. Vyvenko, T. Arguirov, W. Seifert, I. Zizak, M. Trushin and M. Kittler, *Phys. Status Solidi A*, 2010, **207**, 1940–1943.
29 A. Sakdinawat and D. Attwood, *Nat. Photonics*, 2010, **4**, 840–848.
30 M. Trushin, W. Seifert, O. Vyvenko, J. Bauer, G. Martinez-Criado, M. Salome and M. Kittler, *Nucl. Instrum. Methods Phys. Res., Sect. B*, 2010, **268**, 254–258.
31 S. McHugo, A. Thompson, A. Mohammed, G. Lamble, I. Perichaud, S. Martinuzzi, M. Werner, M. Rinio, W. Koch and H. Hoefs, *J. Appl. Phys.*, 2001, **89**, 4282.
32 T. Buonassisi, M. Heuer, O. Vyvenko, A. Istratov, E. Weber, Z. Cai, B. Lai, T. Ciszek and R. Schindler, *Phys. B*, 2003, **340**, 1137–1141.
33 P. Basore and D. Clugston, *25th IEEE PVSC.*, 1996, 377–381.
34 A. Cottrell, *Proc. R. Soc. London, Ser. A*, 1949, **199**, 104–114.
35 M. Kittler and W. Seifert, *Solid State Phenom.*, 2004, **95–96**, 197–204.
36 M. Kittler, W. Seifert and K. Knobloch, *Microelectron. Eng.*, 2003, **66**, 281–288.
37 Z. Radzimski, T. Zhou, A. Buczkowski, G. Rozgonyi, D. Finn, L. Hellwig and J. Ross, *Appl. Phys. Lett.*, 1992, **60**, 1096–1098.
38 M. M'Hamdi, and E. Olsen, *21st European Photovoltaic Solar Energy Conference*, 2006, 1–4.
39 C. Häßler, G. Stollwerck, W. Koch, W. Krumbe, A. Mller, D. Franke and T. Rettelbach, *Adv. Mater.*, 2001, **13**, 1815–1819.
40 H. Möller, T. Kaden, S. Scholz and S. Würzner, *Appl. Phys. A: Mater. Sci. Process.*, 2009, **96**, 207–220.
41 E. Weber, *Appl. Phys. A: Mater. Sci. Process.*, 1983, **30**, 1–22.
42 W. Cai, V. Bulatov, J. Justo, A. Argon and S. Yip, *Phys. Rev. Lett.*, 2000, **84**, 3346–3349.
43 T. Buonassisi, A. A. Istratov, M. D. Pickett, M. A. Marcus, T. F. Ciszek and E. R. Weber, *Appl. Phys. Lett.*, 2006, **89**, 042102.
44 K. Sumino and M. Imai, *Philos. Mag. B*, 1983, **47**, 753–766.
45 A. Ying, B. Osting, I. Noyan, C. Murray, M. Holt and J. Maser, *J. Appl. Crystallogr.*, 2010, **43**, 587–595.
46 F. S. d'Aragona, *J. Electrochem. Soc.*, 1972, **119**, 948.
47 M. Rinio, S. Peters, M. Werner, A. Lawerenz and H. Moller, *Solid State Phenom.*, 2002, **82–84**, 701–706.